ORIGINAL PAPER

Microstructure and mechanical properties of in situ (TiC + SiC)/ FeCrCoNi high entropy alloy matrix composites

Yu-lu Li[1] · Yue Zhao[1] · Lin Shen[1] · Hao Wu[1] · He-guo Zhu[1]

Abstract

In situ (TiC + SiC) particles (5 vol.% and 10 vol.%, respectively)-reinforced FeCrCoNi high entropy alloy matrix composites were fabricated via vacuum inductive melting method, with equal volume fractions of TiC and SiC particles. X-ray diffraction, scanning electron microscope and energy diffraction spectrum were employed to analyze the microstructure and composition of the samples. The results manifested that the FeCrCoNi matrix is composed of FCC phase, and the in situ particles are homogeneously scattered in the matrix. The presence of reinforcements augmented the ultimate tensile strength from 452 to 783 MPa, and raised the yield strength from 162 to 466 MPa at room temperature, whereas the elongation to fracture was reduced from 70.6% to 28.6%. All the tensile fracture surfaces consisted of numerous tiny dimples, indicating that the composites exhibited ductile fracture. Furthermore, the enhancement of strength ascribes to a combination of thermal mismatch strengthening, load-bearing effect, grain refinement, Orowan strengthening and solid solution strengthening effect, which contribute about 58.0%, 2.4%, 12.3%, 11.1% and 16.2% to the improvement of yield tensile strength, respectively.

Keywords High entropy alloy matrix composite · In situ reaction · Microstructure · Mechanical property · Strengthening mechanism

1 Introduction

The high entropy alloys (HEAs) [1–3] have been a novel concept for material design proposed in recent years, which were usually composed of four or more elements, wherein the atomic percentage of the constituent elements is 5%–35%. The wear resistance, corrosion resistance, radiation resistance and oxidation resistance of this new alloy are superior to those of traditional alloys. Simultaneously, the mechanical properties can be greatly improved [4, 5]. Actually, the notion of HEAs has long been raised in the last century, but it was not until 2004 that it was valued and developed. Nowadays, many research institutions have begun to carry out related researches on HEAs, including the work on mechanical properties, radiation damage and defect structures [6–8].

In recent years, Ni-based and Co-based alloys have been extensively explored as matrix materials for their brilliant mechanical properties and thermal stability [9–14]. FeCrCoNi alloy, as a quintessential high entropy alloy, is considered to hold outstanding corrosion resistance, high elongation [15] and low creep [16]. Other physical and chemical properties have been extensively studied as well [17, 18]. FeCrCoNi high entropy alloy is a single-phase alloy with a steady FCC structure as previous reports [19, 20]. It is also found that matrix can maintain the thermal stability of the structure at different annealing temperatures [17, 21, 22]. FeCrCoNi high entropy alloy still possesses exceptional strength and promising ductility in extremely low temperature environments [23].

In order to further enhance the mechanical properties of HEAs, certain rare-elements or reinforcement phases are usually added. In situ reaction technology can effectively control the uniformity of particles in the matrix metal, making the interface stable and formidable to be contaminated [24]. On the other facet, the particles can be bound more tightly to the matrix. TiC ceramic particles enjoy the characteristics of high melting point, favorable hardness and impressive chemical stability [25], while SiC particles

✉ He-guo Zhu
   zhg1200@sina.com

1   College of Materials Science and Engineering, Nanjing
    University of Science and Technology, Nanjing 210094,
    Jiangsu, China

own promising wear resistance and high hardness [26]. The mechanical strength, hardness and wear resistance of the matrix can be amended availably by these two kinds of particles under room temperature and high temperature [27].

In this study, in situ (TiC + SiC) particles-reinforced FeCrCoNi high entropy alloys were generated using vacuum inductive melting method. X-ray diffraction (XRD), scanning electron microscopy (SEM) equipped with energy dispersive spectroscopy (EDS) were applied to observe microstructure of samples. The mechanical properties of the samples were measured using electronic universal testing machine. Moreover, the fracture surface morphology was observed through SEM and the strengthening mechanism was analyzed.

2 Experimental procedure

2.1 Methodology

Carbon powders (purity 99.9%, size of 1–5 μm), silicon powders (purity 99.8%, particle size of 30–50 μm), titanium powders (purity 99.8%, particle size of 30–50 μm) and iron powders (purity 99.8%, size of 30–50 μm) were ball-milled in a stainless steel container for 8 h, and then the mixed powders would be dried for 1.5 h. The blended powder was then compressed into cylindrical samples at a pressure of 150 MPa. Subsequently, chromium particles (purity 99.9%), cobalt particles (purity 99.9%) and nickel particles (purity 99.9%) were melted together with the cylindrical samples. The vacuum level of the smelting furnace was set to be 5×10^{-3} Pa, with the argon gas putting into the furnace as a shielding gas with controlling the air pressure at 1.013×10^4 Pa. During the smelting process, the induced current was slowly rose to 550 A. When the pure metal particles and the cylindrical samples were melted, they were dumped into a copper mold and chilled down to room temperature. Regarding the content of each component of the composites, the elements of the high entropy alloy matrix are set as equimolar ratio, and the volume fractions of the two ceramic particles are identical. FeCrCoNi high entropy alloy matrix composites with 0, 5 and 10 vol.% of reinforcing phases are designated as samples A, B and C, individually. The molar ratios of different samples were displayed in Table 1. The microstructure of the specimens was studied

using XRD, SEM and EDS. SiC content and size of grains and particles are detected using Image Pro Plus software.

2.2 Mechanical testing

For the tensile test, the test samples (GB/T 228.1-2010) of each sample were wire-cut by the ingot, and the test was carried out on a UTM/CMT 5000 universal testing machine at a 0.5 mm/min strain rate. The microstructure of the fracture surfaces was observed by SEM and EDS.

3 Results

3.1 XRD analysis

Figure 1 demonstrates XRD spectra of HEAs enhanced by different volume fractions of (TiC + SiC) ceramic particles prepared using vacuum inductive melting method. θ is the glancing angle, i.e., the angle between the incident X-ray and lattice planes, while 2θ represents the diffraction angle. Figure 1a embodies that HEA matrix consists of only an FCC crystal structure and has high peak intensity. With the addition of (TiC + SiC) particles, composites maintain FCC structure although along with a slight shift of peak positions to the left, which may be related to the solid solution phenomena of Si and C elements. Si and C elements can dissolve into the matrix to cause lattice distortion. And the
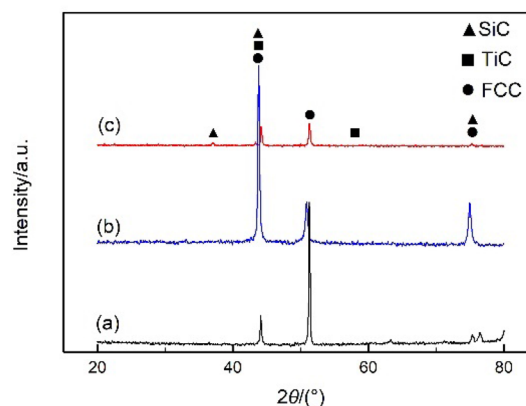

Fig. 1 XRD patterns of FeCrCoNi high entropy alloy. **a** Sample A; **b** sample B; **c** sample C

Table 1 Molar ratios of different fabricated samples

Sample No.	Fe	Cr	Co	Ni	Si	Ti	C
A	1	1	1	1	0	0	0
B	1	1	1	1	0.06	0.06	0.12
C	1	1	1	1	0.12	0.13	0.25

lattice constant becomes larger, resulting in a shift to the left of the peak position. There are peaks of TiC and SiC found in Fig. 1b and c, despite that the corresponding peaks obtained are low due to the little content of particles, which can still verify that TiC and SiC ceramic particles are formed in the high entropy alloy matrix.

3.2 Microstructure

To investigate the distribution of particles, SEM micrographs with EDS spectra of FeCrCoNi high entropy alloy and (TiC + SiC)/FeCrCoNi composites are illustrated in Fig. 2. Figure 2a–c shows SEM images of sample A, sample B and sample C, respectively. EDS analyses of the matrix, TiC and SiC are exhibited in Fig. 2d–f. EDS analysis from the high entropy alloy matrix shows near-equiatomic of Fe, Cr, Co and Ni elements. According to the morphology observation and energy spectrum analysis, the reinforcing phase particles have two kinds of morphological features. One is TiC particles with sharp edges and corners, larger particle size and darker color while the other is SiC particles with smooth shape, smaller size and slightly lighter color. From SEM images, these two kinds of particles both evenly spread in the composites. Comparing Fig. 2b with Fig. 2c, sample C grows denser and the distribution is more uniform with the volume fraction of the reinforcements increasing. In accordance with Fig. 2e, f, Ti content in TiC particles is high, yet the content of the SiC particles is lower than the added content in that a certain amount of Si and C elements can be detected in the matrix. It confirms that the composite

has a phenomenon in which Si and C elements dissolve into the matrix.

Figure 3 exhibits the elemental mapping analysis of sample C which can manifest the distribution of elements directly. The distribution of Si elements in the image can well prove the opinion above, for Si elements are scattered all over the matrix. However, there are still some marginally brighter positions indicating the higher concentration of Si elements, and that are the region of SiC particles. The distribution images of other elements demonstrate that Ti elements centralize in the particles, C elements are present in particles and boundaries, and Fe, Cr, Co and Ni elements primarily exist in the matrix. Moreover, the grain boundaries are rich in Cr elements, which presents a phenomenon of Cr segregation [28].

It is a clear observation of the grain boundaries, distribution and size of the particles from the corroded samples. SEM micrographs of three samples after etching and EDS spectrum of the grain boundary are exhibited in Fig. 4. As can be seen from Fig. 4a–c, the grains are obviously refined after adding various volume fractions of reinforcements. Moreover, the grain size is becoming finer and the boundaries are more twisted with the amplification of the volume fractions of ceramic particles, which is a significant strengthening mechanism of the composites. The reinforcing phases are distributed both at the grain boundary and within the grain. Nevertheless, combined with Fig. 3, the particles are distributed around the boundaries. And TiC and SiC particles spread evenly within the grain. According to SEM images, TiC
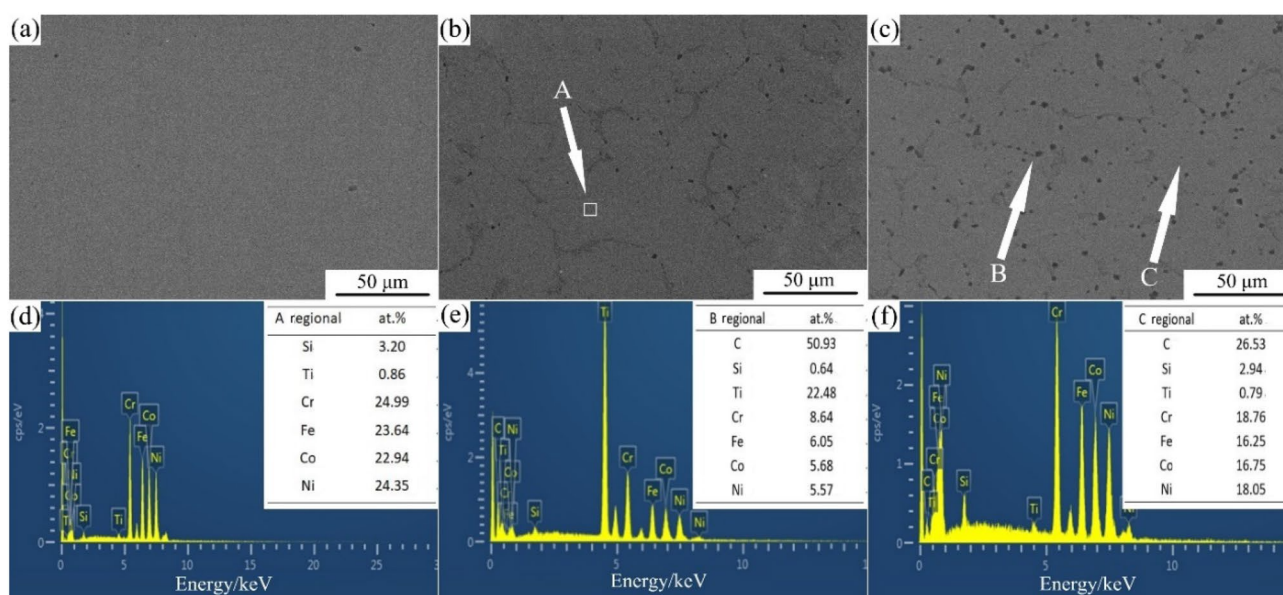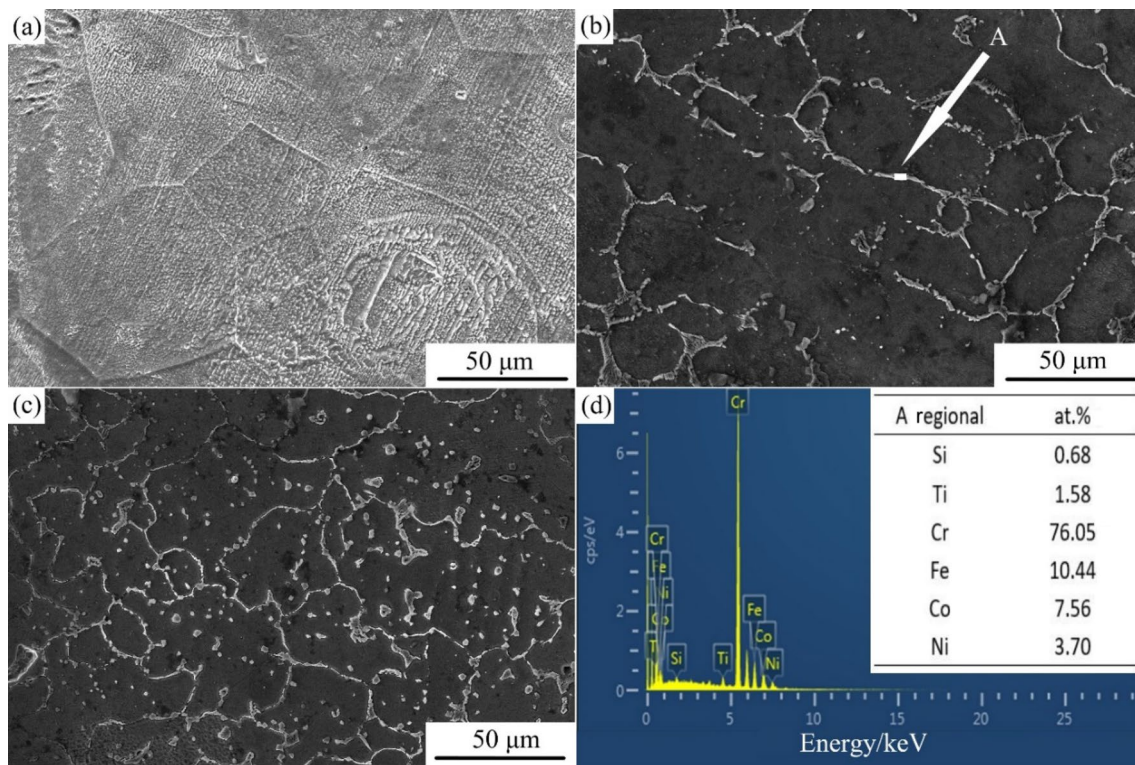

Fig. 2 SEM micrograph (**a**–**c**) and EDS spectrum (**d**–**f**) of FeCrCoNi high entropy alloy before corrosion. **a** Sample A; **b** sample B; **c** sample C; **d** region A; **e** point B; **f** point C

Fig. 3 Elemental mapping analysis of sample C
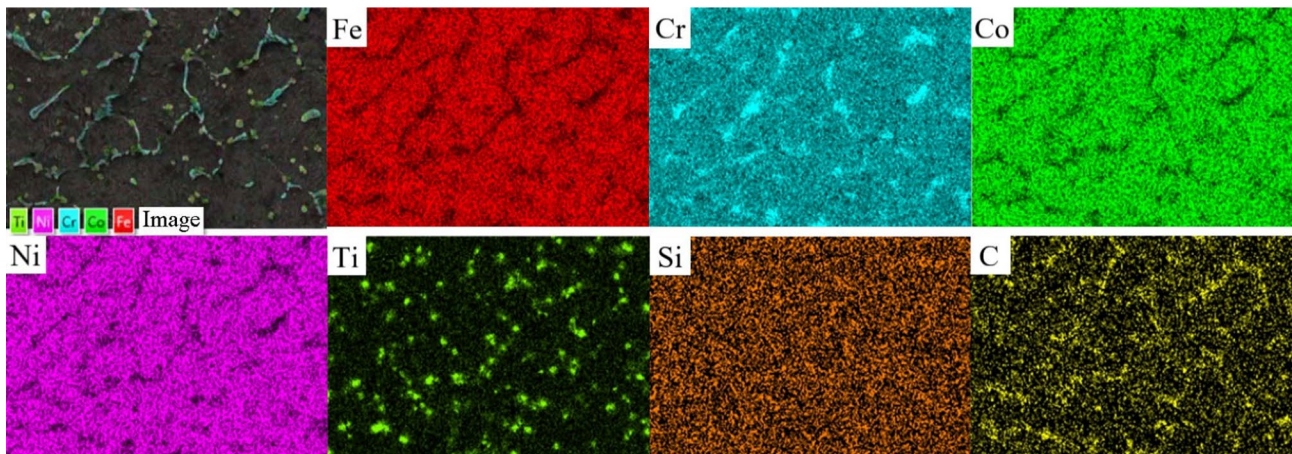
A regional	at.%
Si	0.68
Ti	1.58
Cr	76.05
Fe	10.44
Co	7.56
Ni	3.70

Fig. 4 SEM micrograph (**a–c**) and EDS spectrum (**d**) of FeCrCoNi high entropy alloy after corrosion. **a** Sample A; **b** sample B; **c** sample C; **d** region A in **b**

particles are generally larger, while SiC particles are tiny compared with TiC. At the same time, since Si elements are dissolved into the matrix, the volume fractions of SiC phases look fractionally less than that of TiC phases. Figure 4d shows the element contents of the white square area A in Fig. 4b, and the high content of Cr elements which reaches 76.05% verifies the phenomenon of Cr segregation on the boundaries. Figure 5 shows the grain size of the matrix and composite, and the size of the particles is also demonstrated. Under the measurement, the sizes of the matrix, composite, TiC and SiC are found to be 47.91, 13.68, 2.15 and 0.76 μm, severally. Moreover, SiC content of sample C is detected to be 3.2% by using Image Pro Plus software.
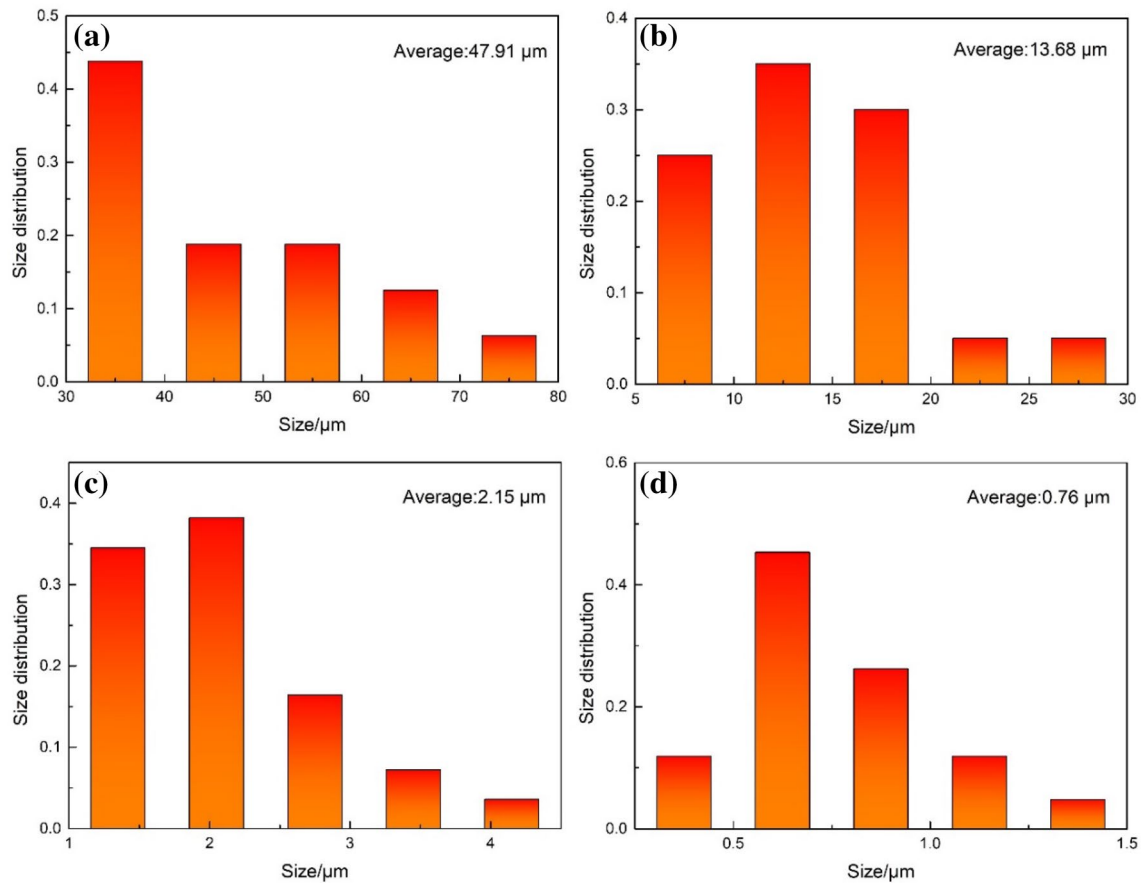
Fig. 5 Size distribution of sample A (**a**), sample C (**b**), TiC particles (**c**) and SiC particles (**d**)
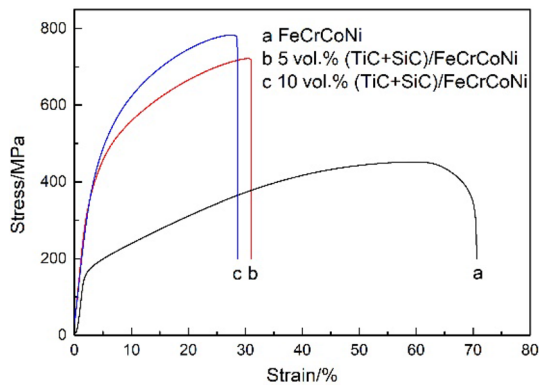
Fig. 6 Engineering stress–strain curves of composites with different volume fractions of reinforcement phases

3.3 Mechanical properties

The engineering stress–strain curves of the composites at room temperature are exhibited in Fig. 6, which embodies the ultimate tensile strength and elongation of samples A, B and C. In order to compare intuitively, Table 2 summarizes the mechanical properties of the samples. From the

Table 2 Mechanical properties of high entropy alloy composites at room temperature

Sample No.	Yield tensile strength/MPa	Ultimate tensile strength/MPa	Elongation/%
A	162	452	70.6
B	420	722	31.0
C	466	783	28.6

curve and chart, the elongation of sample A is 70.6%, which is consistent with the description of excellent ductility of FeCrCoNi high entropy alloy by previous reports [27, 29]. Nevertheless, the ultimate tensile strength and the yield tensile strength of high entropy alloy only reaches 452 and 162 MPa, respectively. To enhance the strength of HEA, the ceramic particles can be added in matrix. The higher the volume fractions of particles put in, the more evident increment of ultimate tensile strength and yield tensile strength will be obtained, at the expense of the decrease of elongation. The ultimate tensile strength of samples B and C is 722 and 783 MPa, respectively, which is 59.73% and 73.23% higher than that of the matrix. As for yield tensile strength, samples

B and C gain 159.25% and 187.65% improvement compared with sample A, while the elongations of samples B and C are 31.0% and 28.6%, respectively.

Figure 7 presents SEM micrographs of the fracture surfaces of samples A, B and C. From Fig. 7, there are many tiny dimples at the surfaces of three samples, suggesting that the composites are all ductile fracture. Ceramic particles can be detected in the dimples of both samples B and C, indicating a strong interfacial combination between the particles and the matrix, which have a positive effect on the increase in ultimate tensile strength. Besides, the dissolution of Si elements contributes to exalting the mechanical properties as well, which causes the lattice distortion of crystal lattice to block the movements of dislocations. From Fig. 7b, c, the structures of the composites are determined to be dendritic.

4 Discussion

With the addition of TiC and SiC reinforcement phases, the mechanical properties of HEAs have been enhanced, which may be related to the following five strengthening mechanisms: thermal mismatch strengthening, load-bearing effect, grain refinement, Orowan strengthening, and solid solution strengthening.

4.1 Thermal mismatch strengthening

Thermal mismatch strengthening is the most typical dislocation strengthening, and it is also a common strengthening mechanism. This mechanism resulted from the diversity in thermal expansion coefficient between the reinforcements and the matrix alloys. During the temperature change of the composites, the thermal deformation of the reinforcement phases and the matrix is inconsistent as well. This results in residual stresses in the matrix around the particles, which leads to the increase in dislocation density that in turn raises the resistance to the dislocation slip, thus enhancing the yield tensile strength of the composites. The calculation can be denoted as follows [30]:

$$\Delta\sigma_{CTE} = \alpha Gb\sqrt{\frac{12\Delta T\Delta Cf_v}{bd_p}} \tag{1}$$

where $\Delta\sigma_{CTE}$ denotes the alteration of yield strength induced by thermal mismatch strengthening; α is a constant (~1.25 [30]); G means the shear modulus of the matrix (~86 GPa [31]); b stands for the burgers vector (~0.253 nm [32]); ΔT represents the discrepancy between room temperature (~293 K) and treatment temperature; ΔC denotes the mismatch between the thermal expansion coefficients of the matrix and the particles; and f_v and d_p represent the volume
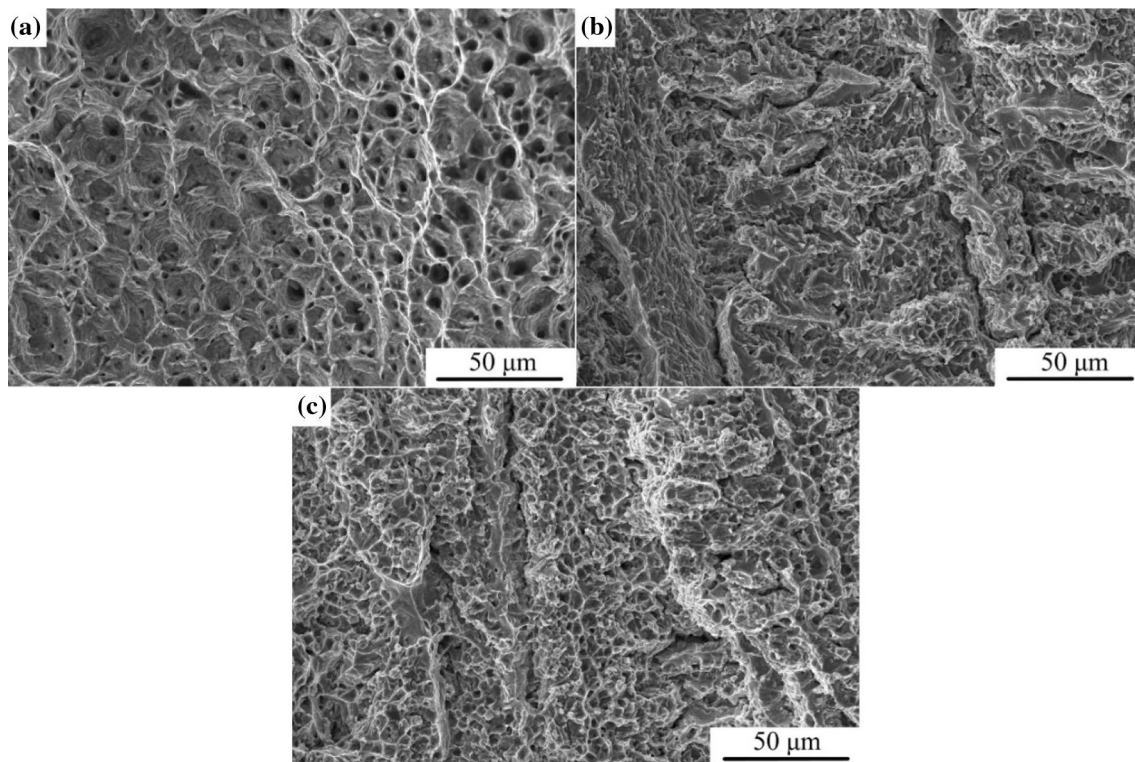
Fig. 7 Tensile fractured surface morphology of sample A (**a**), sample B (**b**) and sample C (**c**)

fraction and average particle diameter of reinforcements. The coefficients of thermal expansion (CTE) of SiC and TiC are 4.3×10^{-6} [33] and 7.74×10^{-6} K^{-1} [25], respectively, and CTE of the matrix is 0 approximately [34]. For the processing temperature, TiC is 1442 K [25], and SiC is 1233 K [35]. As can be seen from the data above, there is a gap in CTE between the matrix and the particles, which raises dislocation density in the matrix near the particles more likely to occur when temperature changes, thereby contributing to the increment of yield tensile strength.

4.2 Load-bearing effect

Actually, when the composites are subjected to external loads, the reinforcements suffer most loads, which results in an increment in the yield tensile strength of the composites after adding the ceramic particles. Simultaneously, with the expansion of the volume fraction of the particles, the enhancement of yield tensile strength of composites is more significant, so that the load-bearing effect is a crucial performance enhancement factor in this experiment. The equation is as follows [36]:

$$\Delta\sigma_{\text{load}} = 0.5 V_{\text{p}} \sigma_{\text{m}} \tag{2}$$

where $\Delta\sigma_{\text{load}}$ represents an increment in the yield tensile strength of the composites because of load-bearing effect; σ_{m} means the yield tensile strength of the matrix (~162 MPa); and V_{p} is the volume fraction of the reinforcement particles. On the basis of the yield strength of the matrix, the data of the augmentation effect of the load-bearing enhancement mechanism of the reinforcements in different volume fractions can be calculated, as demonstrated in Table 3. According to the stress–strain curve, the yield strength of composites is higher with the volume fractions of the reinforcements getting larger.

4.3 Grain refinement

Grain refinement is a strengthening mechanism via refining the grain size to heighten the strength of the metal. In alloys and composites, the grain boundaries are usually high-angle grain boundaries. When the adjacent grains with different orientations are subject to plastic deformation in virtue of external forces, the dislocation sources

in the grains will start to move and slip along the crystal planes. When sliding to the grain boundaries, they will be blocked and cannot be transferred to the adjacent grains, resulting in dislocation accumulation in the grains. Therefore, when the grains become finer, and the grain boundaries get larger and more tortuous, the propagation of cracks in the crystal becomes more unfavorable. This leads to the amelioration of the yield tensile strength of composite materials. In term of Hall–Petch relationship, the correlation of grain size and yield tensile strength of the composites can be obtained [37]:

$$\sigma_y = \sigma_0 + k_y d^{-1/2} \tag{3}$$

where σ_y stands for the yield tensile strength of the composites; σ_0 means the lattice frictional stress of the material; k_y is the strengthening coefficient (~276 [38]); and d is the mean grain size. However, the Hall–Petch relationship of high entropy alloys has also been proposed [39]. Based on the original formula, they modified the meaning of the parameters, and defined σ_0 as the intrinsic hardness of high entropy alloys, so that the strengthening effect of the composites on hardness can be computed by Hall–Petch relationship [40]. By observing Fig. 4a–c, it can be found that the crystal grains of the composites are obviously finer after the addition of the particles; likewise, the grain size of the sample with the reinforcement volume fraction of 10% is also significantly finer than that of the sample with the volume fraction of 5%.

4.4 Orowan strengthening

Orowan strengthening is defined that in the case that plastic deformation occurs, the slip dislocation is blocked by the particles in the alloy, and the dislocation line cannot directly cut through the second-phase particles. However, under acted upon by an external force, the dislocation line will bypass the particles leaving dislocation loops around the reinforcements [33, 41]. The bending of the dislocation lines results in the distortion of the surrounding crystal lattice, improving the lattice distortion energy of the crystal. Thereby, it can develop the resistance of the dislocation slippage, and finally the tensile strength of the alloy rises. From SEM micrographs of Fig. 4, it can be seen that there are some reinforcements particles with a grain size of less than 1 μm in the alloy, and the Orowan strengthening is generally considered as a strengthening mechanism only of great significance to the alloy when the size of particles is less than 1 μm. Even though the volume fraction of the particles is considered to be small, Orowan strengthening mechanism can still function [42, 43]. The Orowan mechanism can be calculated by the following equation [44]:

Table 3 Strengthening effect of load-bearing effect on composites

Sample No.	Volume fraction of (TiC+SiC)/%	$\Delta\sigma_{\text{load}}$/MPa
B	5	3.4
C	10	6.7

$$\Delta \sigma_{\text{Orowan}} = M \cdot \frac{0.4Gb}{\pi \sqrt{1-\nu}} \cdot \frac{\ln\left(\frac{\sqrt{\frac{2}{3}}d}{b}\right)}{\sqrt{\frac{2}{3}}d\left(\sqrt{\frac{\pi}{4V_{\text{p}}}} - 1\right)} \quad (4)$$

where $\Delta\sigma_{\text{Orowan}}$ means the change of yield strength owing to Orowan strengthening; M stands for the Taylor factor (~3.06 [32]); and ν represents the Poisson's ratio (~0.25 [31]). The volume fraction of particles should refer to that of SiC due to the large size of TiC particles and the large spacing among the particles. At this work, the effect of the Orowan strengthening mechanism on TiC particles is not obvious.

4.5 Solid solution strengthening

Solid solution strengthening underlies the phenomenon in which the tensile strength and hardness of pure metal tend to be enhanced after suitable alloying process [45, 46]. This is because some of the alloy elements can dissolve in the matrix and trigger lattice distortion, which raises the obstruction against dislocation motion, thus enhancing the tensile strength and hardness of the alloy (i.e., solid solution). The effect of solid solution strengthening on composites can be counted as follows [47]:

$$\Delta\sigma_{\text{s}} = M\frac{Gc^{1/2}\varepsilon_{\text{S}}^{3/2}}{700} \quad (5)$$

where $\Delta\sigma_{\text{s}}$ is the increase in yield strength of composites caused by elemental dissolution; c is the molar ratio of the reinforcing phase in the material; and ε_{S} is the interaction parameter, which is approximately equal to the parameter ε_{a} that can be easily obtained from the refined XRD pattern. $\frac{\varepsilon_{\text{S}}^{3/2}}{700}$ can approximately equal to 1.3×10^{-3} for the lack of proper data [35]. It can be seen from Fig. 3 that some Si elements do not combine with C elements to form SiC particles, which are dissolved into the matrix. Thus, the more Si element dissolves into the matrix, the clearer the impact of this strengthening mechanism on the composites.

The final yield tensile strength of sample C, $\sigma_{0.1}$, can be calculated by summing results above with σ_0, which can be expressed as follows [37]:

$$\sigma_{0.1} = \sigma_0 + \Delta\sigma_{\text{CTE}} + \Delta\sigma_{\text{load}} + \Delta\sigma_y + \Delta\sigma_{\text{Orowan}} + \Delta\sigma_{\text{s}} \quad (6)$$

And the theoretical value is given as:

$$\sigma_{0.1} = 162 + 164 + 6.7 + 34.8 + 31.3 + 45.9 = 444.7\,\text{MPa}$$

Thermal mismatch strengthening contributes the most to the amelioration of yield tensile strength, accounting for 58.0%. The other four strengthening mechanisms mentioned above take up 2.4%, 12.3%, 11.1% and 16.2%, respectively.

For SiC, it owns a greater influence on the strengthening, which takes up 62.0%. Compared with the experimental result of the composites (466 MPa), the theoretical result (444.7 MPa) has little difference, which may come from the deviation in the volume fraction and size of SiC particles.

5 Conclusions

1. FeCrCoNi high entropy alloy is FCC structure. After adding the reinforcements, the high entropy alloy still maintains FCC structure. There is Cr segregation at the grain boundary, and some Si elements are dissolved into the matrix. Moreover, TiC and SiC particles are evenly distributed on the matrix.
2. After reinforcements are added in matrix, the grain of the composites is obviously refined, and the grain refining effect becomes increasingly significant as the volume fraction of the reinforcements extends.
3. When the volume fraction of the reinforcements heightens, the ultimate tensile strength of the composite enhances accompanied by the elongation decreasing. The ultimate tensile strength of sample C is 783 MPa, which is an increase in 73.3% related to the matrix, and the yield tensile strength get rise from 162 to 466 MPa, while the elongation falls down from 70.6% to 28.6%.
4. Thermal mismatch strengthening, load-bearing effect, grain refinement, Orowan strengthening and solid solution strengthening are the primary strengthening contributors in the composites, which devote 58.0%, 2.4%, 12.3%, 11.1% and 16.2% to the overall strength increase, respectively.

References

[1] J.W. Yeh, S.K. Chen, S.J. Lin, J.Y. Gan, T.S. Chin, T.T. Shun, C.H. Tsau, S.Y. Chang, Adv. Eng. Mater. 6 (2004) 299–303.
[2] J.W. Yeh, S.Y. Chang, Y.D. Hong, S.K. Chen, S.J. Lin, Mater. Chem. Phys. 103 (2007) 41–46.
[3] J.W. Yeh, Ann. Chim. Sci. Mater. 1 (2006) 633–648.
[4] H. Wu, S.R. Huang, C.Y. Zhu, H.G. Zhu, Z.H. Xie, Mater. Lett. 257 (2019) 126729.
[5] X.R. Zhang, J. Guo, X.H. Zhang, Y.P. Song, Z.X. Li, X.F. Xing, D. Kong, J. Alloy. Compd. 775 (2019) 565–570.
[6] D. Yim, P. Sathiyamoorthi, S.J. Hong, H.S. Kim, J. Alloy. Compd. 781 (2019) 389–396.

[7] C.M. Barr, J.E. Nathaniel, K.A. Unocic, J.P. Liu, Y. Zhang, Y.Q. Wang, M.L. Taheri, Scripta Mater. 156 (2018) 80–84.

[8] A. Heczel, M. Kawasaki, J.L. Lábár, J. Jang, T.G. Langdon, J. Gubicza, J. Alloy. Compd. 711 (2017) 143–154.

[9] X.L. Shi, J. Yao, Z.S. Xu, W.Z. Zhai, S.Y. Song, M. Wang, Q.X. Zhang, Mater. Des. 53 (2014) 620–633.

[10] W.B. Duan, Y.H. Sun, C.H. Liu, S.H. Liu, Y.Y. Li, C.H. Ding, G. Ran, L. Yu, Tribol. Int. 95 (2016) 324–332.

[11] J. Chen, X.Y. Zhou, W.L. Wang, B. Liu, Y.K. Lv, W. Yang, D.P. Xu, Y. Liu, J. Alloy. Compd. 760 (2018) 15–30.

[12] J.X. Hou, M. Zhang, H.J. Yang, J.W. Qiao, Y.C. Wu, Mater. Lett. 238 (2019) 258–260.

[13] H. Shahmir, M. Nili-Ahmadabadi, A. Shafiee, M. Andrzejczuk, M. Lewandowska, T.G. Langdon, Mater. Sci. Eng. A 725 (2018) 196–206.

[14] A.J. Zhang, J.S. Han, B. Su, J.H. Meng, J. Alloy. Compd. 725 (2017) 700–710.

[15] Y.F. Kao, T.J. Chen, S.K. Chen, J.W. Yeh, J. Alloy. Compd. 488 (2009) 57–64.

[16] M.A. Hemphill, T. Yuan, G.Y. Wang, J.W. Yeh, C.W. Tsai, A. Chuang, P.K. Liaw, Acta Mater. 60 (2012) 5723–5734.

[17] B.L. Zhang, Y. Zhang, S.M. Guo, J. Mater. Sci. 53 (2018) 14729–14738.

[18] B. Gludovatz, E.P. George, R.O. Ritchie, JOM 67 (2015) 2262–2270.

[19] M. Vaidya, S. Trubel, B.S. Murty, G. Wildea, S.V. Divinskia, J. Alloy. Compd. 668 (2016) 994–1001.

[20] X.T. Song, R.P. Guo, Z. Wang, X.J. Wang, H.J. Yang, J.W. Qiao, L.N. Han, P.K. Liaw, Y.C. Wu, Intermetallics 114 (2019) 106591.

[21] J.X Hou, X.H. Shi, J.W. Qiao, Y. Zhang, P.K. Liaw, Y.C. Wu, Mater. Des. 180 (2019) 107910.

[22] F. He, Z.J. Wang, Q.F. Wu, J.J. Li, J.C. Wang, C.T. Liu, Scripta Mater. 126 (2017) 15–19.

[23] J.P. Liu, X.X. Guo, Q.Y. Lin, Z.B. He, X.H. An, L.F. Li, P.K. Liaw, X.Z. Liao, L.P. Yu, J.P. Lin, L. Xie, J.L. Ren, Y. Zhang, Sci. China Mater. 62 (2019) 853–863.

[24] X.F. Du, T. Gao, G.L. Liu, X.F. Liu, J. Alloy. Compd. 695 (2017) 1–8.

[25] X.D. Sun, H.G. Zhu, J.L. Li, J.W. Huang, Z.H. Xie, Mater. Chem. Phys. 220 (2018) 449–459.

[26] Y. Yu, W.M. Liu, T.B. Zhang, J.S. Li, J. Wang, H.C. Kou, J. Li, Metall. Mater. Trans. A 45 (2014) 201–207.

[27] L. Rogal, D. Kalita, A. Tarasek, P. Bobrowski, F. Czerwinski, J. Alloy. Compd. 708 (2017) 344–352.

[28] W. Fang, H.Y. Yu, R.B. Chang, X. Zhang, P.G. Ji, B.X. Liu, J. Li, X.H. Qu, Y. Liu, F.X. Yin, Mater. Chem. Phys. 238 (2019) 121897.

[29] Q.C. Fan, B.S. Li, Y. Zhang, Mater. Sci. Eng. A 598 (2014) 244–250.

[30] J.C. Li, X.X. Zhang, L. Geng, Composit. Part A Appl. Sci. Manufact. 121 (2019) 487–498.

[31] G. Laplanche, P. Gadaud, C. Bärsch, K. Demtröder, C. Reinhart, J. Schreuer, E.P. George, J. Alloy. Compd. 746 (2018) 244–255.

[32] Y.Q. Wang, B. Liu, K. Yan, M.S. Wang, S. Kabra, Y.L. Chiu, D. Dye, P.D. Lee, Y. Liu, B. Cai, Acta Mater. 154 (2018) 79–89.

[33] X.Z. Zhang, T.J. Chen, Mater. Sci. Eng. A 696 (2017) 466–477.

[34] D.B. Miraclea, O.N. Senkov, Acta Mater. 122 (2017) 448–511.

[35] H. Wu, S.R. Huang, H. Qiu, H.G. Zhu, Z.H. Xie, Sci. Rep. 9 (2019) 16356.

[36] H. Li, X.M. Wang, L.H. Chai, H. Wang, Z. Chen, Z. Xiang, T. Jin, Mater. Sci. Eng. A 720 (2018) 60–68.

[37] H. Cheng, W. Chen, X.Q. Liu, Q. Tang, Y. Xie, P. Dai, Mater. Sci. Eng. A 719 (2018) 192–198.

[38] S. Yoshida, T. Ikeuchi, T. Bhattacharjee, Y. Bai, A. Shibata, N. Tsuji, Acta Mater. 171 (2019) 201–215.

[39] W.H. Liu, Y. Wu, J.Y. He, T.G. Nieh, Z.P. Lu, Scripta Mater. 68 (2013) 526–529.

[40] P. Sathiyamoorthi, J. Basu, S. Kashyap, K.G. Pradeep, R.V. Kottada, Mater. Des. 134 (2017) 426–433.

[41] S. Amirkhanlou, M. Rahimian, M. Ketabchi, N. Parvin, P. Yaghinali, F. Carreno, Metall. Mater. Trans. A 47 (2016) 5136–5145.

[42] X.Z. Zhang, T.J. Chen, Y.H. Qin, Mater. Des. 99 (2016) 182–192.

[43] Y.K. Kim, J.H. Choe, K.A. Lee, J. Alloy. Compd. 805 (2019) 680–691.

[44] X. Liu, L. Zhang, Y. Xu, Appl. Phys. A 123 (2017) 567.

[45] C.R. LaRosa, M. Shih, C. Varvenne, M. Ghazisaeidi, Mater. Charact. 151 (2019) 310–317.

[46] X.L. Ding, Y.Z. Zhan, H.Q. Tang, JOM 71 (2019) 3473–3480.

[47] J.W. Wan, B. Liu, C.T. Liu, Y. Liu, Intermetallics 102 (2018) 58–64.